RSC Advances

PAPER

View Article Online
View Journal | View Issue

Cite this: *RSC Adv.*, 2026, **16**, 23625

Ag–Sn@MOFs heterostructure enables ultrasensitive voltammetric determination of vismodegib in serum and urine

Glowi Alasiri,[a] Ali M. Alaseem,[b] Razan Orfali,[b] Ramadan Ali,[c] Al-Montaser Bellah H. Ali[d] and Mohamed M. El-Wekil *[de]

Accurate measurement of vismodegib (VIS) is essential for pharmacokinetic profiling, individualized dosing, and therapeutic drug monitoring. In this work, we report an Ag–Sn@MOFs heterostructure as a sustainable composite sensing interface for highly sensitive voltammetric determination of VIS. A simple solvothermal – reduction route yielded an integrated nanocomposite that synergistically combines the high conductivity and electrocatalytic activity of Ag nanoparticles with the high-surface-area, defect-rich architecture of Sn@MOFs. Multimodal characterization verified uniform immobilization of Ag nanoparticles on the Sn@MOFs scaffold and the formation of a stable, conductive interface. Owing to accelerated charge-transfer kinetics and enhanced VIS oxidation, the modified electrode delivered an ultralow limit of detection of 0.006 nM, high sensitivity of 14.782 μA nM^{-1} cm^{-2}, and a wide linear range of 0.05–500 nM (R^2 = 0.9974). Importantly, the sensor maintained excellent accuracy in complex matrices, providing recoveries of 95.6–107.6% with precision ≤3.29% RSD in spiked human urine and serum, demonstrating strong matrix tolerance. The combination of scalable, low-toxicity fabrication with robust selectivity and stability highlights the platform's potential for VIS therapeutic monitoring, pharmacokinetic studies, and translation toward point-of-care diagnostics.

Received 7th March 2026
Accepted 27th April 2026

DOI: 10.1039/d6ra01976e

rsc.li/rsc-advances

1. Introduction

Cancer results from accumulated molecular alterations that deregulate cell proliferation, differentiation, and survival, enabling autonomous clonal expansion. It may present as solid tumors or as disseminated hematologic malignancies (*e.g.*, leukemias) without a discrete mass.[1,2] Malignant cells invade adjacent tissues and often metastasize, a major cause of cancer mortality, reflecting hallmark capabilities such as sustained growth signaling, evasion of suppressors, resistance to cell death, replicative immortality, angiogenesis, and invasion/metastasis, enabled by genome instability and tumor-promoting inflammation[3]. Vismodegib (VIS; ERIVEDGE®) is an oral Smoothened (SMO) inhibitor for adults with locally advanced or metastatic basal cell carcinoma (BCC) when surgery and/or radiotherapy are not appropriate.[4] BCC is commonly driven by aberrant Hedgehog (Hh) signaling, which—despite being largely inactive in adult tissues—can be pathologically reactivated by PTCH1 loss or activating SMO mutations, leading to constitutive transcriptional signaling and tumor growth. By inhibiting SMO, VIS suppresses Hh signaling and produces meaningful clinical responses in advanced disease.[5] Quantifying VIS in pharmaceutical and biological matrices is justified by nonlinear pharmacokinetics due to saturable absorption and high-affinity, saturable protein binding, as well as a boxed warning for embryo-fetal toxicity and serious cutaneous and musculoskeletal adverse effects. Sensitive, selective methods support quality control, PK studies, and exposure assessment to minimize toxicity while maintaining therapeutic levels.[6]

VIS has been determined in biological matrices predominantly by hyphenated chromatographic platforms, most notably LC-MS/MS (including approaches that quantify unbound drug after equilibrium dialysis and extract clean-up) and, for quality-control applications, by reversed-phase HPLC or (U)PLC-based stability-indicating assays.[7–10] Although these methods provide excellent sensitivity and robustness, they typically require capital-intensive instrumentation and nontrivial sample preparation (*e.g.*, protein precipitation and/or SPE/LLE workflows) to mitigate matrix effects—factors that increase per-sample cost and can constrain throughput in routine or decentralized

[a]*Department of Biochemistry, College of Medicine, Imam Mohammad Ibn Saud Islamic University (IMSIU), Riyadh, 13317, Saudi Arabia*

[b]*Department of Pharmacology College of Medicine, Imam Mohammad Ibn Saud Islamic University (IMSIU), Riyadh 13317, Saudi Arabia*

[c]*Department of Pharmaceutical Chemistry, Faculty of Pharmacy, University of Tabuk, Tabuk 71491, Saudi Arabia*

[d]*Department of Pharmaceutical Analytical Chemistry, Faculty of Pharmacy, Assiut University, Assiut, 71526, Egypt. E-mail: mohamed.elwakeel@pharm.aun.edu.eg; mohamed.mohamoud@ymail.com*

[e]*Pharmaceutical Chemistry Department, Faculty of Pharmacy, Badr University in Assiut (BUA), 2014101, Assiut, Egypt*

testing.[11,12] In contrast, electrochemical methods offer major advantages for chemical and biosensing because they are typically fast, sensitive, and low-cost, while requiring minimal sample preparation and small sample volumes.[13,14]

Metal–organic frameworks (MOFs) offer highly tunable architectures with exceptionally high surface areas and well-defined, controllable pore sizes, which enables dense loading of active sites and efficient mass transport within their porous networks.[15] Their intrinsic electrical conductivity—often a limitation for electrochemical applications—can be improved through strategies such as metal-ion doping that modulate charge-carrier density and facilitate electron transport pathways.[16] Moreover, constructing metal nanoparticle-MOF composites typically yield a synergistic enhancement, where the nanoparticles provide fast electron-transfer channels and additional catalytic sites while the MOF scaffold preserves high porosity and prevents particle agglomeration, resulting in higher effective conductivity and accessible surface area than pristine MOFs.[17] Silver nanoparticle–MOF composites are widely used as electrode modifiers in electrochemical detection because they combine the MOF's high surface area/porosity (to preconcentrate analytes and expose many active sites) with AgNPs' high electrical conductivity and strong electrocatalytic activity (to accelerate charge transfer and amplify current signals).[18,19] In practice, AgNPs can be incorporated by *in situ* reduction of Ag^+ within/onto the MOF or by post-synthetic deposition, producing synergistic effects: (i) lower charge-transfer resistance and higher peak currents, (ii) improved sensitivity and lower LODs *via* faster electron-transfer kinetics and more accessible catalytic sites, and (iii) enhanced stability because the MOF scaffold helps disperse/anchor AgNPs and limits agglomeration.

In this work, we report a new electrochemical sensing architecture for VIS based on a silver-decorated tin-containing metal–organic framework (Ag–Sn@MOF). The Sn@MOF scaffold was constructed *via* a solvothermal route using terephthalic acid as the organic linker to generate a porous coordination network with abundant adsorption/interaction sites. Subsequently, Ag nanoparticles (Ag) were immobilized onto/within the MOF by *in situ* chemical reduction, yielding a heterostructured composite in which the conductive Ag domains are intimately coupled to the MOF matrix. Comprehensive physicochemical characterization was performed to confirm successful framework formation and Ag incorporation, including verification of crystallinity and phase composition, pore architecture/surface area, and surface functional groups. Electrochemical interrogation by cyclic voltammetry (CV) and electrochemical impedance spectroscopy (EIS) demonstrated markedly enhanced interfacial electron-transfer kinetics and reduced charge-transfer resistance after Ag loading, consistent with the formation of efficient conductive pathways and synergistic catalytic sites arising from the Ag–Sn@MOF composite. Building on these findings, VIS was quantified using differential pulse voltammetry (DPV), which provided well-resolved oxidation responses suitable for trace analysis. Method applicability in complex biofluids was evaluated through standard-addition recovery experiments in spiked human urine and serum, confirming matrix tolerance and practical feasibility for real-sample testing. Overall, the proposed Ag–Sn@MOF platform integrates (i) high surface area/porosity for analyte preconcentration, (ii) catalytic/charge-transport enhancement from Ag NPs, and (iii) favorable electrochemical signal transduction, supporting its potential as a rapid and cost-effective alternative to instrument-intensive chromatographic assays for VIS monitoring.

2. Experimental

2.1. Materials and reagents

VIS (~99%), carboplatin (~99%), cisplatin (~98%), dopamine (~97%), glycine (~98%), glutathione (~98%), cysteine (~99%), flutamide (~98%), ascorbic acid (~97%), uric acid (~98%), cytarabine (~99%), fludarabine (~98%), methionine (~98%), glucose (~98%), Nafion, bovine serum albumin, and terephthalic acid (TA, ~98%) were purchased from Sigma-Aldrich (Germany). Acetonitrile, methanol, *N*,*N*-dimethylformamide (DMF), silver nitrate ($AgNO_3$), tin(II) chloride dihydrate ($SnCl_2 \cdot 2H_2O$), potassium ferricyanide ($K_3[Fe(CN)_6]$), potassium ferrocyanide ($K_4[Fe(CN)_6]$), potassium chloride (KCl), sodium dihydrogen phosphate (NaH_2PO_4), disodium hydrogen phosphate (Na_2HPO_4), sodium hydroxide (NaOH), and hydrochloric acid (HCl) were obtained from Merck (Germany).

2.2. Preparation of stock and working solutions of VIS standard

VIS (MW = 421.3 g mol^{-1}) was accurately weighed (4.213 mg) and dissolved in acetonitrile/water (1 : 1, v/v) in a 10.0 mL volumetric flask. The solution was sonicated for 10 min to ensure complete dissolution, then stored at 4 °C in a dark glass vial. A 1 : 100 dilution was performed by transferring 100 μL of the 1.0 mM stock into a 10.0 mL volumetric flask and diluting to the mark with 0.1 M phosphate buffer (pH 7.0) containing 1% acetonitrile to maintain solubility. All working solutions were freshly prepared daily by serial dilution of the 10.0 μM intermediate stock using 0.1 M phosphate buffer (pH 7.0). For instance, 50 μL of 10.0 μM VIS was diluted to 10.0 mL with phosphate buffer to obtain 50 nM VIS.

2.3. Synthesis Sn@MOF

A tin-based metal–organic framework (Sn@MOF) was prepared using a solvothermal protocol adapted from the literature.[20] Briefly, equimolar amounts of $SnCl_2 \cdot 2H_2O$ (5.0 mM) and terephthalic acid (5.0 mM) were dissolved in a mixed DMF/ethanol solvent (25 mL) and magnetically stirred for 3 h to obtain a homogeneous precursor solution. The mixture was then transferred to a Teflon-lined stainless-steel autoclave and heated at 120 °C for 12 h. After cooling to room temperature, the resulting solid was collected by centrifugation, washed thoroughly with DMF and ethanol to remove residual reagents and unreacted linker, and finally dried at 80 °C for 8 h prior to further use.

2.4. Synthesis of Ag–Sn@MOF

Ag nanoparticles were deposited onto Sn@MOF by an *in situ* reduction approach. In a typical preparation, Sn@MOF (0.85 g)

was ultrasonically dispersed in deionized water for 30 min, after which 10 mL of $AgNO_3$ solution (0.5 M) was introduced under continuous stirring and the mixture was stirred for 1 h. Hydrazine monohydrate was then added dropwise to adjust the pH to 9–10, followed by the addition of $NaBH_4$ (0.5 g) to complete Ag^+ reduction; stirring was continued for a further 1 h. The resulting Ag–Sn@MOF composite was collected by centrifugation and washed repeatedly (6000 rpm, 20 min, three cycles) to remove residual ions and reducing agents, then dried at 70 °C for 5 h. To optimize Ag loading, the $AgNO_3$ concentration was systematically varied over 0.05–0.60 M while keeping other parameters constant.

2.5. Preparation of Ag–Sn@MOF/GCE

Prior to surface functionalization, the glassy carbon electrode (GCE) was mechanically polished using alumina slurry, thoroughly rinsed with deionized water, and finally wiped with ethanol to remove residual particulates and organic contaminants. For electrode modification, Ag–Sn@MOF was dispersed in isopropanol containing Nafion and ultrasonicated to obtain a homogeneous suspension. An aliquot of the resulting ink was drop-cast onto the pretreated GCE surface and allowed to dry at ambient conditions for 3 h to yield the Ag–Sn@MOF/GCE.

2.6. Calculation of recoveries % and RSD %

The relative standard deviation (RSD%) was calculated to assess the precision of the analytical measurements. For each sample, the mean concentration was first calculated by averaging the found concentrations of the spiked samples. The standard deviation (SD) was then calculated, which measures the spread or variability of the measurements. The RSD% was calculated using the formula:

$$\mathrm{RSD}\% = \frac{\mathrm{SD}}{\mathrm{mean}} \times 100$$

The recovery % was calculated to determine the accuracy of the analytical method in quantifying the spiked VIS in both serum and urine matrices. The recovery was calculated using the formula:

$$\mathrm{Recovery}\% = \frac{\mathrm{Found}}{\mathrm{spiked}} \times 100$$

3. Results and discussions

3.1. Structural and morphological characterization

Multiple electron-microscopy techniques were employed to elucidate the morphology and microstructure of the as-prepared composites. As shown in Fig. 1A, pristine Sn@MOF exhibits a well-defined rod-like architecture with relatively smooth surfaces. After silver loading (Fig. 1B), the MOF rods become decorated with densely distributed Ag nanoparticles, appearing as brighter/agglomerated domains on the Sn@MOF surface, which evidences successful nanoparticle deposition. The corresponding TEM image (Fig. 1C) further confirms the formation of nanoscale Ag particles with a narrow size distribution and an average diameter of 6.78 nm. The HRTEM inset reveals clear lattice fringes with an interplanar spacing of 0.26 nm, indicating high crystallinity and supporting the generation of metallic Ag nanocrystallites anchored to the Sn@MOF scaffold.[21] Elemental composition was verified by EDX analysis. Fig. 1D presents the EDX spectrum of Ag–Sn@MOFs, displaying characteristic signals of C, O, and N from the organic framework, alongside distinct peaks corresponding to Sn and Ag, confirming the coexistence of the MOF matrix and

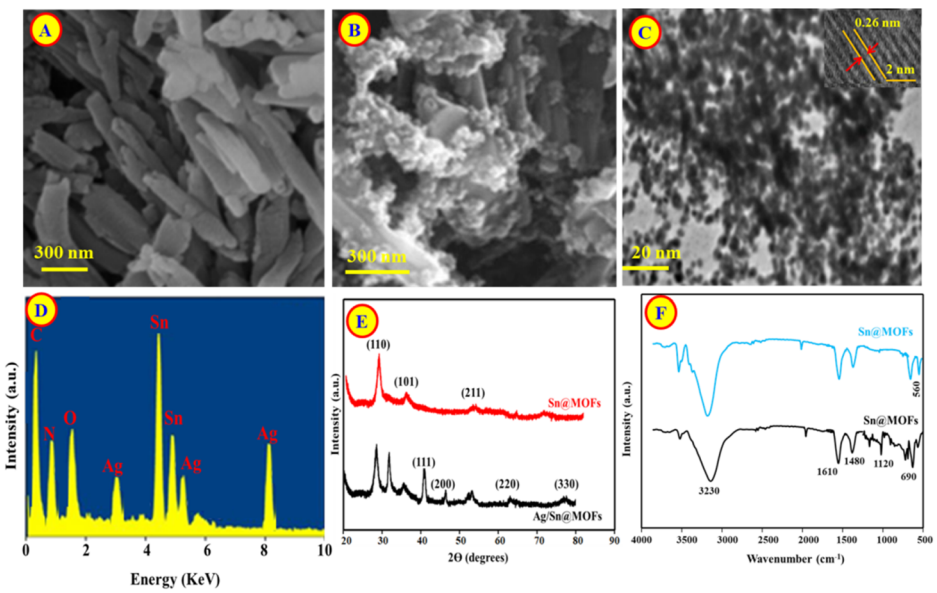

Fig. 1 (A) SEM image of Sn@MOFs; (B) SEM image of Ag–Sn@MOFs; (C) TEM image of Ag nanoparticles (inset is high resolution TEM); (D) EDX of Ag–Sn@MOFs; (E) XRD pattern of Sn@MOFs and Ag–Sn@MOFs; (F) FTIR spectra of Sn@MOFs and Ag–Sn@MOFs.

Ag in the final composite and supporting the effective incorporation of Ag onto Sn@MOFs.

Fig. 1E compares the XRD patterns (2θ = 15–80°) of Sn@MOFs and Ag–Sn@MOFs. The diffraction features of Sn@MOFs, with reflections at 27.8°, 35.7°, and 53.4°, are consistent with the previously reported assignments to the (110), (101), and (211) planes, confirming the preservation of the Sn-based crystalline framework.[22,23] Upon Ag decoration, additional reflections emerge at 40.2°, 45.7°, 63.6°, and 78.7°, which can be indexed to the face-centered cubic phase of metallic Ag corresponding to the (111), (200), (220), and (330) planes (JCPDS 01-087-0597).[24,25] The appearance of these Ag-specific peaks, together with the retained Sn@MOFs reflections, evidences successful incorporation of Ag nanoparticles without disrupting the host MOF structure. The average crystallite size of the Ag domains was estimated using the Debye–Scherrer relation to be approximately 10.5 nm.[26]

Fig. 1F presents the FTIR spectra of Sn@MOF and Ag–Sn@MOF. For pristine Sn@MOF, the characteristic bands at 3230, 1610, 1480, 1120, and 690 cm^{-1} are assigned to O–H/N–H stretching, C=O/C=N stretching, aromatic C=C vibrations, C–O stretching, and Sn–O vibrations, respectively, in agreement with previous reports.[27] After Ag nanoparticle decoration, an additional absorption band appears at ~560 cm^{-1}, which can be attributed to Ag–O stretching, indicating the presence of Ag-related vibrational features in the composite. Importantly, the principal Sn@MOF bands remain essentially unchanged in position, suggesting that the framework's functional groups and coordination environment are largely preserved after Ag loading. This observation supports that Ag nanoparticles are primarily immobilized on the MOF surface without inducing substantial chemical modification of the host lattice.[28]

Fig. S1A and S1B show the N_2 adsorption–desorption isotherms of Sn@MOFs and Ag–Sn@MOFs. Both samples exhibit type IV behavior accompanied by an H3 hysteresis loop over the relative pressure range (P/P_0 ≈ 0.2–1.0), which is characteristic of mesoporous materials and is commonly associated with slit-like pores arising from aggregated plate-/rod-like particles.[29] In line with this textural signature, pristine Sn@MOFs display a BET specific surface area of 33.5 $m^2\ g^{-1}$ and a total pore volume of 0.016 $cm^3\ g^{-1}$. After Ag loading, these values increase to 44.3 $m^2\ g^{-1}$ and 0.042 $cm^3\ g^{-1}$, respectively, indicating that the surface-accessible porosity is enhanced in the composite. Consistently, the BJH-derived average pore diameter increases from 3.42 to 5.78 nm, suggesting a shift toward larger mesopores. Collectively, the increased surface area and enlarged mesoporous channels are expected to facilitate electrolyte penetration and reduce diffusion constraints, which can contribute to improved electrochemical kinetics and signal output, as reported for related porous electrode architectures.[30]

XPS was employed to verify the surface elemental composition and chemical states of the Ag–Sn@MOFs composite. The wide-scan spectrum (Fig. 2A; 0–1000 eV) reveals the presence of C, N, O, Sn, and Ag, confirming successful incorporation of Ag within the Sn@MOFs matrix. In the high-resolution C 1s spectrum (Fig. 2B), the component at 284.4 eV is assigned to C–C/C=C species, while the contribution at 285.9 eV is attributed to carbonyl-related bonding (C=O), consistent with the organic linker environment.[31] A single N 1s signal centered at 398.5 eV is observed (Fig. 2C), indicating a uniform nitrogen chemical environment associated with the MOF framework.[32] The O 1s region (Fig. 2D) can be deconvoluted into two main contributions at 530.8 and 531.5 eV, corresponding to C–O and C=O oxygen functionalities, respectively, further supporting the retention of the MOF organic coordination motifs after Ag loading.[33] The Ag 3d spectrum (Fig. 2E) displays two well-defined peaks at 367.8 eV (Ag $3d_{5/2}$) and 373.9 eV (Ag $3d_{3/2}$).

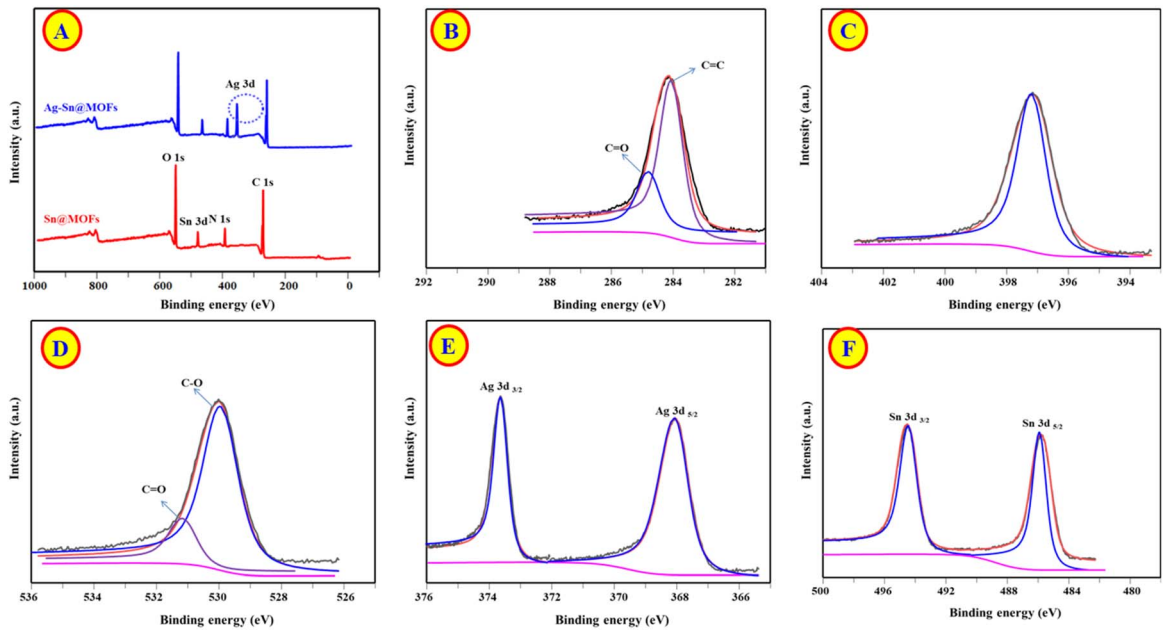

Fig. 2 (A) XPS full spectra of Sn@MOFs and Ag–Sn@MOFs; (B–F) High resolution spectra of C 1s, N 1s, O 1s, Ag 3d, and Sn 3d.

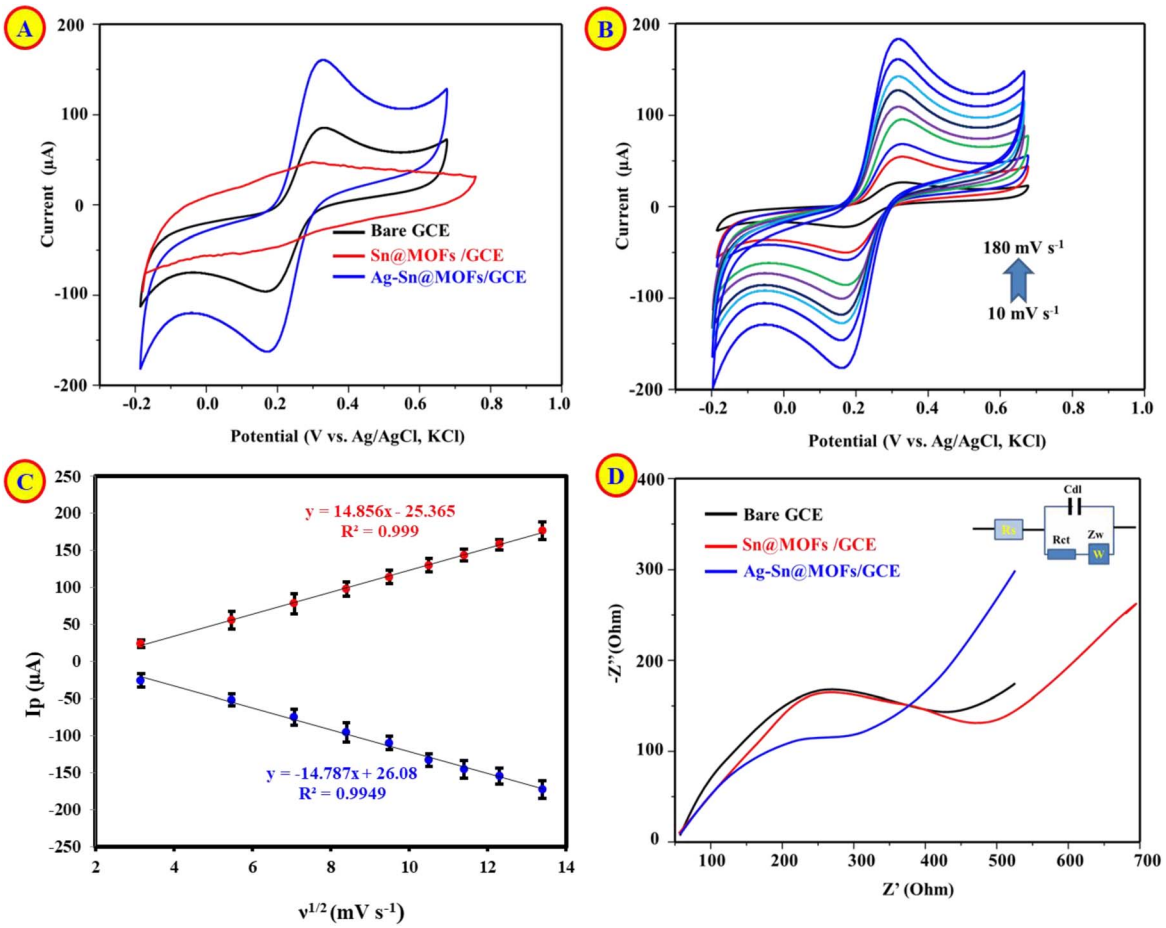

Fig. 3 Electrochemical characterization of modified electrodes: (A) CV comparison bare GCE, Sn@MOFs/GCE, and Ag–Sn@MOFs/GCE. (B) CVs of Ag–Sn@MOFs/GCE at 10–180 mV s^{-1}. (C) Linear dependence of oxidation peak current on square root of scan rate. (D) EIS Nyquist plots in 5.0 mM $[Fe(CN)_6]^{3-/4-}$ containing 0.1 M KCl.

Their binding energies and the spin–orbit splitting of ~6.1 eV is characteristic of metallic Ag (Ag^0), corroborating that silver is predominantly present as zerovalent nanoparticles rather than oxidized silver species.[34] In addition, the Sn 3d spectrum (Fig. 2F) exhibits peaks at 486.2 eV (Sn $3d_{5/2}$) and 495.2 eV (Sn $3d_{3/2}$), which are consistent with Sn(IV), confirming that the tin nodes retain their oxidized state within the MOF framework.[35]

Thermal stability and framework integrity were evaluated by TGA (Fig. S2). Pristine Sn@MOF exhibited an initial weight loss of ~15.18% below 150 °C, attributed to desorption of water and residual DMF/ethanol. A second major weight loss of ~48.67% between 330 °C and 440 °C corresponds to decomposition of the terephthalic acid linker and collapse of the MOF structure. The residual mass at ~600 °C is consistent with SnO_2 formation. For Ag–Sn@MOF, a similar decomposition profile was observed, but the onset of linker decomposition shifted slightly to higher temperature, suggesting that Ag nanoparticles impart modest thermal stabilization to the framework, likely due to interfacial interactions. The residual mass increased to ~38.87 wt%, in good agreement with the Ag loading estimated from EDX and XPS. Importantly, no additional decomposition steps were observed, confirming that the MOF structure remains intact after Ag incorporation under the mild synthesis conditions used. These TGA results, together with XRD, confirm that Ag–Sn@MOF is thermally stable up to at least 390 °C, far exceeding any operating temperature encountered during electrochemical measurements.

3.2. Electrochemical characterization

Fig. 3A compares the CVs of bare GCE, Sn@MOFs/GCE, and Ag–Sn@MOFs/GCE recorded in 5.0 mM $[Fe(CN)_6]^{3-/4-}$ containing 0.1 M KCl (−0.2 to 0.8 V *vs.* Ag/AgCl). Relative to bare GCE, Sn@MOFs/GCE displays attenuated anodic/cathodic peak currents, indicating hindered interfacial electron transfer. The reduced electrochemical response of pristine Sn@MOF/GCE compared to bare GCE arises from the intrinsic semiconducting nature of the carboxylate-linked Sn-MOF, which acts as a passivating layer that increases charge-transfer resistance and limits access of the $[Fe(CN)_6]^{3-/4-}$ probe. This behavior is consistent with many non-conductive MOFs and contrasts with prior reports where enhanced activity was achieved *via* pyrolysis, conductive additives, or alternative morphologies.[36] In contrast, Ag–Sn@MOFs/GCE exhibits markedly enhanced redox peak currents, evidencing accelerated charge-transfer kinetics

and improved electroactive accessibility. The Ag incorporation likely establishes conductive pathways and additional catalytic sites, thereby promoting more efficient electron shuttling of the $[Fe(CN)_6]^{3-/4-}$ and overall electrocatalytic performance.

To probe the interfacial kinetics, cyclic voltammograms of Ag–Sn@MOFs/GCE were acquired at scan rates from 10 to 180 mV s^{-1} (Fig. 3B). The anodic/cathodic peak currents exhibited a linear dependence on the square root of the scan rate (Fig. 3C), consistent with a predominantly diffusion-controlled redox process for the $[Fe(CN)_6]^{3-/4-}$ probe under the employed conditions. The electrochemically active surface areas values were estimated using the Randles–Sevcik relationship (at the relevant temperature and assuming reversible behavior).[37,38] The calculated EASA increased from 0.032 cm^2 (bare GCE) to 0.068 cm^2 (Ag–Sn@MOFs/GCE), whereas Sn@MOFs/GCE showed a reduced EASA of 0.011 cm^2, suggesting partial surface blocking and/or limited conductivity upon MOF deposition. Collectively, these findings indicate that Ag incorporation not only restores but enhances the electroactive interface, providing more accessible sites and facilitating electron transport, which rationalizes the improved electroanalytical response.

Electrochemical impedance spectroscopy (EIS) was employed to quantify interfacial charge-transfer resistance (R_{ct}). Nyquist spectra (Fig. 3D) were acquired in 5.0 mM $[Fe(CN)_6]^{3-/4-}$ containing 0.1 M KCl and fitted using a Randles equivalent circuit (inset). The extracted R_{ct} values increased from 800.78 Ω for bare GCE to 1600.65 Ω after Sn@MOFs modification, consistent with impeded electron transport and/or partial surface blocking by the MOF layer. Notably, Ag incorporation markedly reduced R_{ct} to 287.54 Ω for Ag–Sn@MOFs/GCE, evidencing accelerated charge-transfer kinetics and improved interfacial conductivity. This impedance trend corroborates the CV results, collectively confirming that Ag deposition effectively restores and enhances electron transfer across the electrode/electrolyte interface.

Electrochemical oxidation of VIS was probed by CV at bare GCE, Sn@MOFs/GCE, and Ag–Sn@MOFs/GCE (Fig. S3A). Among the tested electrodes, Ag–Sn@MOFs/GCE delivered the largest anodic peak current, evidencing a pronounced electrocatalytic enhancement toward VIS oxidation relative to bare GCE and Sn@MOFs/GCE. Under the employed conditions, VIS exhibited an irreversible oxidation peak centered at ~0.908 V (*vs.* Ag/AgCl), indicating non-reversible charge-transfer behavior and suggesting kinetic limitations and/or a coupled follow-up chemical step. The superior response of Ag–Sn@MOFs/GCE is consistent with its improved interfacial electron-transfer properties observed in the redox-probe characterization (CV/EIS) and its higher electroactive accessibility.

3.3. Optimization of conditions

The loading of Ag–Sn@MOFs on the GCE was systematically optimized by varying both the suspension concentration and the drop-cast volume to maximize the electrocatalytic response. Increasing the Ag–Sn@MOFs concentration progressively enhanced the anodic peak current, reaching an optimum at 6.0 mg mL^{-1} (Fig. S3B). This enhancement is consistent with a higher density of accessible catalytic sites and the formation of more effective conductive pathways that facilitate interfacial

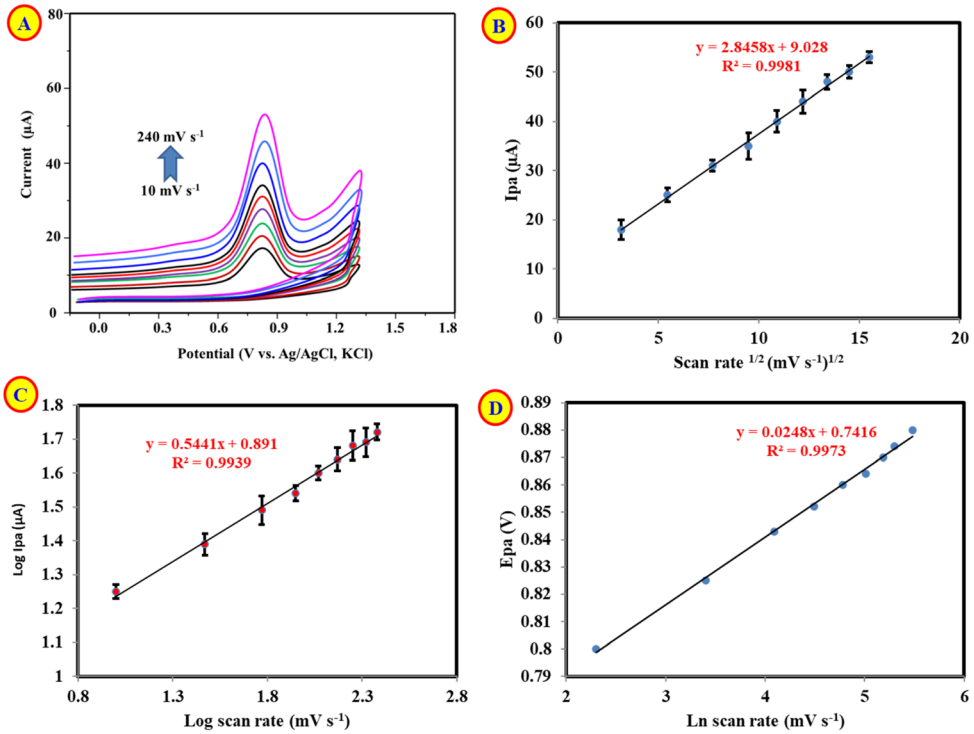

Fig. 4 Scan-rate study for VIS (5.0 µM): (A) CVs at 10–240 mV s^{-1}. (B) Linear dependence of I_{pa} on square root of scan rate. (C) log–log plot of I_{pa} *vs.* ν. (D) Laviron plot (E_{pa} *vs.* ln ν). Error bars represent SD of triplicate measurements ($n = 3$).

electron transfer. However, further increases in loading led to a decline in current, which can be rationalized by particle agglomeration and the development of an excessively thick/compact film that partially blocks electroactive sites and imposes diffusion and charge-transport limitations. Accordingly, 6.0 mg mL^{-1} was selected as the optimal loading concentration for subsequent measurements.

The deposition volume was further optimized by drop-casting 3–15 μL of the Ag–Sn@MOFs dispersion (6.0 mg mL^{-1}) onto the GCE surface (Fig. S3C). The anodic peak current increased with increasing volume and reached a maximum at 10 μL, indicating improved electroactive coverage and a higher density of accessible catalytic sites. At larger volumes, the current decreased, which is plausibly attributed to the formation of an overly thick/compact film that introduces diffusion barriers and increases charge-transfer resistance, thereby impeding mass transport and electron transfer. Accordingly, a dispersion concentration of 6.0 mg mL^{-1} and a deposition volume of 10 μL were selected as the optimized conditions for fabricating Ag–Sn@MOFs/GCE in subsequent experiments.

The $AgNO_3$ concentration used for Ag incorporation was optimized based on the DPV response toward VIS oxidation (Fig. S3D). The anodic peak current increased with $AgNO_3$ concentration and reached its maximum at 0.35 M, indicating the most effective balance between Ag-site formation and interfacial conductivity under the studied conditions. At concentrations beyond this optimum, the response did not improve further (or decreased), likely due to excessive Ag deposition that can promote particle coalescence and/or generate a denser layer that partially blocks electroactive sites and hinders mass/charge transport.[17] Therefore, 0.35 M $AgNO_3$ was selected as the optimal concentration for subsequent electrode preparation.

CVs acquired over 10–240 mV s^{-1} (Fig. 4A) show a progressive positive shift in the VIS anodic peak potential (E_{pa}) with increasing scan rate, a hallmark of an irreversible (or quasi-irreversible) oxidation in which electron-transfer kinetics cannot fully track the imposed potential sweep.[39] In parallel, the anodic peak current (I_{pa}) increased linearly with the square root of scan rate ($I_{pa} = 2.845\ \nu^{1/2} + 9.028$, $R^2 = 0.9981$; Fig. 4B). The equation $I_{pa} = 2.845\nu^{1/2} + 9.028$ describes the linear relationship between the anodic peak current (I_{pa}) and the square root of the scan rate ($\nu^{1/2}$) in CV experiments. This relationship is characteristic of a diffusion-controlled process, where the rate of the electrochemical reaction is primarily governed by the diffusion of the analyte (VIS) to the electrode surface. The slope of 2.845 reflects the diffusion behavior and can be used to estimate parameters such as the diffusion coefficient and electrochemical surface area, while the intercept of 9.028 indicates the baseline current. This linear dependence further confirms that the oxidation of VIS is not limited by adsorption or surface interactions but is controlled by the diffusion of the analyte towards the electrode. These findings suggest efficient mass transport and validate the assumption of diffusion-controlled kinetics in this electrochemical setup.[40,41] The absence of current saturation across the investigated scan-rate window further argues against significant site-limited adsorption behavior. Consistently, the log (I_{pa})–log (ν) dependence (Fig. 4C) yielded a slope of 0.5441 ($R^2 = 0.9939$), close to the theoretical value of ~0.5 expected for diffusion-controlled kinetics, confirming that VIS oxidation is governed mainly by mass transport rather than adsorption or other surface-limited pathways.[42]

The excellent linearity of the scan-rate diagnostics indicates that VIS oxidation remains governed by a uniform diffusion regime across the investigated window, with no clear evidence of mixed control or adsorption-dominated behavior. To further extract kinetic parameters for the irreversible oxidation step, Laviron's treatment was applied to the dependence of the anodic peak potential on scan rate, using the $E_{pa}/\ln \nu$ relationship (Fig. 4D). From the fitted slope (which is proportional to $RT/(\alpha\ nF)$ for an irreversible process), the charge-transfer coefficient α was obtained, consistent with irreversible electron transfer under the employed conditions; the analysis further indicated that the number of electrons involved in the rate-limiting step is approximately two (Scheme 1). These results are in line with the systematic positive shift of E_{pa} at higher scan rates, which reflects kinetic limitations relative to the applied potential sweep.

The effect of solution pH on VIS oxidation was systematically examined, revealing a maximum anodic peak current at pH 7.0 followed by a gradual decrease at higher pH values (Fig. 5A). This trend is consistent with reduced proton availability and less favorable proton-coupled charge-transfer kinetics under more alkaline conditions. Notably, the anodic peak potential (E_{pa}) shifted linearly toward less positive values as pH increased (Fig. 5B), with an average slope of ~−59 mV per pH unit. Such a near-Nernstian pH dependence indicates involvement of an equal number of protons and electrons in the rate-determining redox step, supporting a $2H^+/2e^-$ proton-coupled electron-transfer process for VIS oxidation under the investigated conditions.[43,44] The pyridine ring is proposed as the primary site of VIS oxidation based on substantial literature precedent.

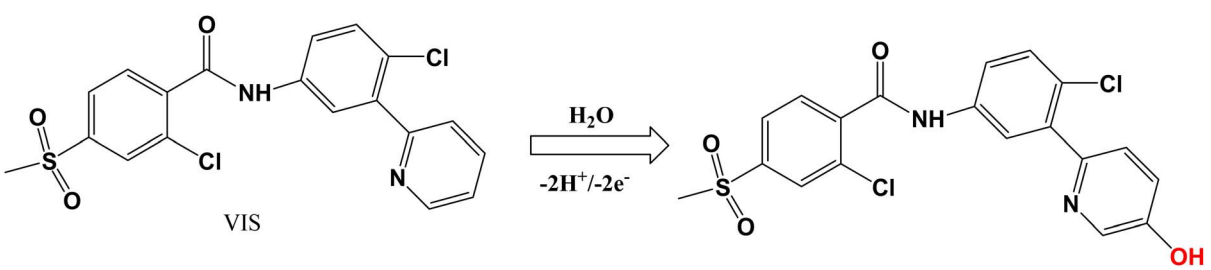

Scheme 1 Possible oxidation mechanism for VIS electrochemical oxidation at Ag–Sn@MOFs/GCE.

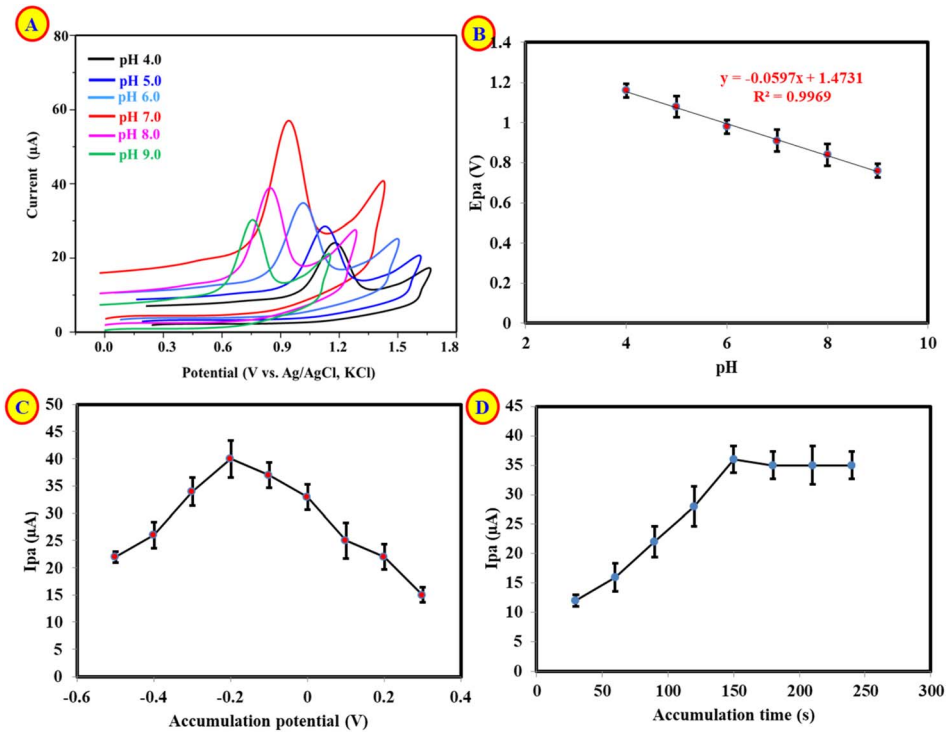

Fig. 5 Effect of pH on VIS (50 nM) oxidation at Ag–Sn@MOFs/GCE: (A) CV curves recorded from pH 4.0 to 9.0. (B) E_{pa}–pH calibration plot. Effect of accumulation potential (C) and time (D) on the oxidation of 50 nM VIS. Error bars represent SD of triplicate measurements ($n = 3$).

Metabolism studies of VIS have consistently demonstrated that the pyridine moiety undergoes cytochrome P450-mediated oxidation, leading to ring-opened metabolites (M9, M13, M18) *via* aldehyde intermediates.[45,46] Stable isotope labeling ($^{13}C_2$, ^{15}N) confirmed that the pyridine nitrogen is retained in these oxidative products, establishing the pyridine ring as the redox-active center. The other aromatic rings in VIS—the central chlorophenyl and terminal methylsulfonylphenyl—are electron-deficient and significantly less susceptible to electrochemical oxidation under the mild conditions employed (pH 7.0, ~0.9 V *vs.* Ag/AgCl). The observed $2H^+/2e^-$ mechanism (pH slope −59 mV pH^{-1}) is consistent with the initial formation of a radical cation at the pyridine nitrogen, followed by deprotonation and further oxidation, analogous to known electrochemical behavior of pyridine-containing pharmaceuticals.

The effect of varying the concentration of VIS on anodic currents was investigated and presented in Fig. S4. It was observed that increasing the concentration of VIS led to a corresponding increase in the anodic currents within the concentration range of 5–90 μM. A linear regression analysis yielded the equation $I_{pa}(\mu A) = 1.3455\ [VIS] + 5.7967$ ($R^2 = 0.9987$), demonstrating a strong linear relationship between anodic current and VIS concentration. The LOD was determined to be 1.67 μM, indicating the sensor's high sensitivity within this concentration range.

In addition, the accumulation conditions were systematically optimized by examining both accumulation potential and accumulation time (Fig. 5C and D). The VIS oxidation response increased as the accumulation potential was varied and reached its maximum at −0.2 V, indicating the most favorable balance between analyte enrichment at the electrode interface and preservation of an electroactive surface. Likewise, the peak current increased with accumulation time up to 150 s, after which no further improvement was observed, consistent with saturation of available adsorption/enrichment sites and/or partial surface blocking at longer times. Accordingly, an accumulation potential of −0.2 V and an accumulation time of 150 s were selected as the optimal preconcentration parameters to maximize the sensor sensitivity in subsequent determinations.

3.4. Analytical performance and figures of merit

DPV measurements performed in 0.1 M phosphate buffer (pH 7.0) demonstrated that the Ag–Sn@MOFs/GCE provides a robust electroanalytical readout for VIS over the 0–500 nM range (Fig. 6A). VIS generated a sharp, irreversible oxidation peak centered at ~0.887 V (*vs.* Ag/AgCl), and the anodic peak current increased proportionally with VIS concentration, yielding the calibration equation: $I_{pa}(\mu A) = 0.3108[VIS] + 17.243$ with excellent linearity ($R^2 = 0.9974$) (Fig. 6B). The LOD was calculated using the signal-to-noise ratio method, where the noise level was determined from five replicate DPV measurements of the blank (phosphate buffer). The standard deviation of the blank current at the VIS oxidation potential (~0.887 V) was 0.62 nA. Using the calibration slope of 0.3108 μA nM^{-1}, the LOD (S/N = 3) was calculated as (3 × 0.00062 μA)/(0.3108 μA nM^{-1}) = 0.006 nM. Notably, an ultralow detection limit of 0.006 nM (S/N = 3) was obtained, underscoring the capability of the modified electrode to transduce trace-level VIS into a measurable faradaic signal. The enhanced response is

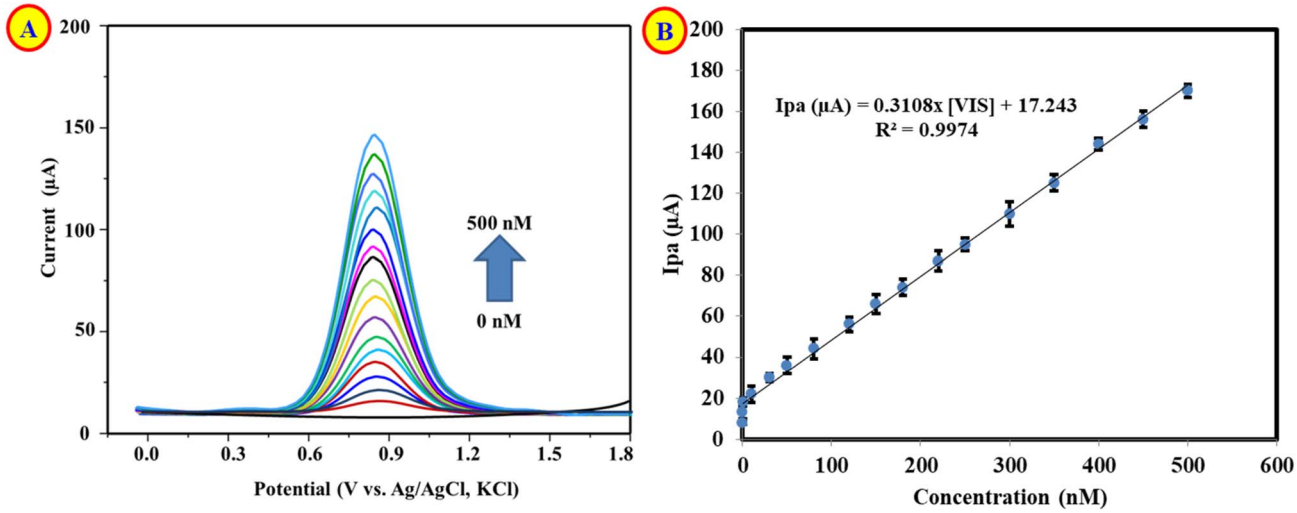

Fig. 6 (A) Concentration-dependent DPV profiles for VIS (0–500 nM) recorded at Ag–Sn@MOFs/GCE and (B) linear calibration relationship. Error bars show SD ($n = 3$).

attributed to the synergistic architecture of the composite: Ag domains facilitate faster electron transport pathways, while the porous Sn–MOF matrix provides abundant adsorption/interaction sites and improves analyte accessibility at the interface. Collectively, these features reduce kinetic limitations at the electrode surface and strengthen the electro-oxidation signal, consistent with the superior DPV sensitivity.

As summarized in Table 1, the Ag–Sn@MOFs/GCE demonstrates competitive-to-superior analytical performance relative to most previously reported VIS sensing platforms, combining a broad working (dynamic) range with an ultralow detection limit. Importantly, such figures of merit support its applicability to trace-level VIS determination in complex matrices, aligning with clinically and environmentally relevant concentration domains. In addition to sensitivity, the practical utility of the sensor is further reinforced by its straightforward electrode fabrication and the rapid DPV readout, which together favor routine implementation and potential translation to point-of-need monitoring.

3.5. Stability and precision

Storage stability was evaluated using three independently prepared Ag–Sn@MOFs/GCE ($n = 3$) stored under dry, dark, desiccated ambient conditions (22–25 °C; 45–55% RH). DPV measurements were recorded in 0.1 M phosphate buffer (pH 7.0) containing 50 nM VIS over a 0–55 day period. The sensors retained 81.55% of their initial peak current after 55 days, accompanied by negligible peak-potential drift (<5 mV) and good signal precision (%RSD <3.84%). Collectively, these results verify the excellent storage robustness of the modified electrodes and support their suitability for long-term use and practical deployment (Fig. S5A). To further assess the stability of the electrode material, XRD analysis was performed after 55 days of storage (Fig. S5B). The results showed that the main peaks retained their original shapes and positions, affirming the structural stability of the composite after this storage period.

Repeatability was examined by performing 40 consecutive DPV measurements at 50 nM VIS using a single Ag–Sn@MOFs/GCE. The anodic peak current exhibited excellent run-to-run consistency (%RSD = 3.08%), while the peak potential remained effectively unchanged (ΔE < 5 mV), indicating minimal signal drift. These results confirm the operational robustness of the electrode and its stable electrocatalytic response during repeated measurements (Fig. S5C).

Fabrication reproducibility was assessed using eight independently prepared Ag–Sn@MOFs/GCE electrodes evaluated under identical DPV conditions ($n = 3$ measurements per electrode). The anodic peak currents showed low electrode-to-electrode variability (%RSD = 3.55%), while the corresponding peak potentials displayed only minor shifts (≤±4 mV). These results confirm excellent inter-electrode consistency, underscoring the reliability of the fabrication procedure and the robustness of the sensing interface (Fig. S5D and S5E).

Table 1 Performance comparison of VIS detection: Ag–Sn@MOFs/GCE *vs.* conventional methods

Technique	Linear range (nM)	LOD (nM)	Reference
LC-MS	0.2–240	—	7
	240–2370		8
RP-HPLC	28 500–285 000	—	9
UPLC	2300–534 400	780	10
Fluorescence	0–340 000	0.4	47
Voltammetry	2500–100 000	750	48
	0–500	0.006	This work

3.6. Selectivity/interference studies

Selectivity and anti-interference performance of the proposed Ag–Sn@MOFs/GCE were systematically evaluated by challenging the sensor with representative inorganic ions (5.0 mM), endogenous/organic biomolecules (1.5 mM), and structurally or

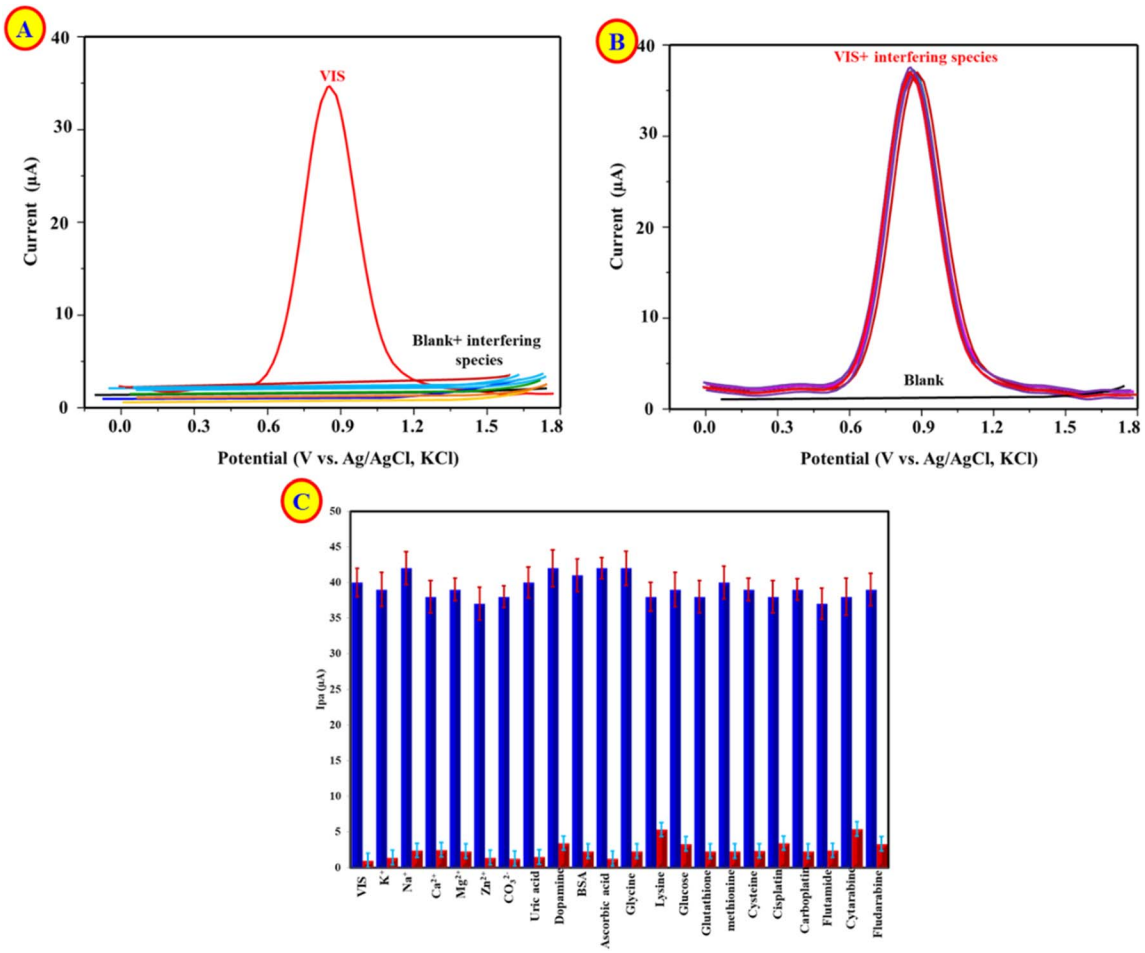

Fig. 7 (A) DPV responses of 50 nM VIS at the Ag–Sn@MOFs/GCE in phosphate buffer (pH 7.0) in the absence and presence of interferents: inorganic ions (5.0 mM), endogenous/organic biomolecules (1.5 mM), anticancer agents (1.0 mM), and BSA (10.0 mg mL^{-1}). (B) Comparison of DPV responses of 50 nM VIS in phosphate buffer (pH 7.0) in the presence of various interferents. (C) Anti-interference performance of the Ag–Sn@MOFs/GCE sensor showing negligible changes in the anodic response in the presence of 5.0 mM inorganic ions, 1.5 mM endogenous/organic biomolecules, and 1.0 mM anticancer agents. Error bars indicate standard deviation ($n = 3$).

pharmacologically related anticancer agents (1.0 mM) under the optimized DPV conditions (Fig. 7). As shown in Fig. 7A, the DPV responses of VIS in the absence and presence of potential interferents are presented, highlighting the sensor's selectivity. Fig. 7B demonstrates the comparison between the responses of VIS and common coexisting ions, showing the interference study results. The anti-interference performance in Fig. 7C further confirms the sensor's ability to distinguish VIS from structurally similar compounds, making it reliable for bioanalytical applications.

In all cases, these potentially coexisting species induced only negligible changes in the anodic response, whereas VIS generated a pronounced oxidation peak/current. This contrast confirms excellent molecular discrimination and high tolerance to common interferents, supporting reliable VIS quantification in complex matrices.

3.7. Applications

The platform's applicability to real biological matrices was assessed by quantifying VIS in spiked human urine and serum. The sensor delivered high recoveries of 96.8–107.6% in urine and 95.6–107.6% in serum, with good precision (%RSD = 2.56–3.29%) (Table 2), demonstrating reliable quantification under physiologically relevant conditions. The absence of noticeable signal suppression after spiking suggests a limited matrix effect and minimal interference from endogenous electroactive constituents. This robustness can be rationalized by the synergistic electrode architecture, where Ag nanoparticles accelerate interfacial electron transfer while the Sn@MOFs scaffold provides a high density of accessible active sites that supports efficient analyte interaction. Importantly, the obtained accuracy and precision fall within widely accepted bioanalytical validation criteria (typically ±15% for QC levels, and ±20% at the LLOQ), supporting the method's suitability for bioanalysis and potential pharmacokinetic applications when complemented by full matrix-effect, stability, and lot-to-lot assessments.

VIS exhibits a therapeutic total plasma concentration range of approximately 2–20 μM (2000–20,000 nM) at steady state, with an unbound (pharmacologically active) fraction of ~0.5–1% (10–200 nM) due to extensive protein binding.[47] In the

Table 2 Determination of VIS in urine and serum samples ($n = 3$)

		Ag–Sn@MOFs/GCE			HPLC-MS/MS[49]		
Matrix	Added (μM)	Found (nM)	Recovery %	RSD %	Found (nM)	Recovery %	RSD %
Serum	0.0	ND	—	—	ND	—	—
	25.0	26.89	107.6	2.56	23.12	92.5	5.28
	50.0	47.80	95.6	3.29	55.73	111.5	4.38
	100.0	104.78	104.8	3.09	96.45	96.5	3.65
Urine	0.0	ND	—	—	ND	—	—
	25.0	24.19	96.8	3.76	27.48	103.6	4.67
	50.0	53.78	107.6	2.56	47.38	109.9	5.52
	100.0	98.72	98.7	3.09	104.32	104.3	4.98

present study, human serum samples were subjected to a 25-fold dilution with phosphate buffer prior to analysis (see SI). This dilution step reduces the expected therapeutic concentrations to 80–800 nM (total) or 0.4–8 nM (free). The sensor's linear range of 0.05–500 nM fully encompasses the diluted therapeutic window for total VIS (80–500 nM) and comfortably covers the free VIS range. For patient samples with total VIS concentrations exceeding 12.5 μM (which would give >500 nM after 25× dilution), a further 2× dilution is recommended to bring the signal within the calibrated range. Thus, the proposed Ag–Sn@MOFs/GCE is well-suited for routine therapeutic drug monitoring of VIS.

4. Conclusions

Ag–Sn@MOFs nanocomposite was synthesized *via* a combined solvothermal growth and chemical reduction strategy and employed to modify GCE for voltammetric determination of VIS. Physicochemical characterization verified the successful anchoring of Ag nanoparticles onto the Sn@MOFs framework, forming a conductive, defect-enriched, and mechanically stable hybrid interface. Relative to the bare GCE and the individually modified counterparts, the Ag–Sn@MOFs/GCE exhibited accelerated interfacial electron-transfer kinetics and an increased electroactive surface area, consistent with improved charge-transport pathways and a higher density of accessible catalytic sites. Under DPV, VIS displayed a wide linear response from 0.05 to 500 nM, with a limit of detection of 0.006 nM (S/N = 3). The analytical gain is attributable to the cooperative electrocatalytic contribution of Ag nanoparticles (facilitating charge transfer) and the Sn@MOFs scaffold (providing abundant active sites and enhanced analyte-surface interaction). The sensing interface also demonstrated practical operational resilience, including good repeatability (RSD 3.08%, 40 consecutive scans) and fabrication reproducibility (RSD 3.55%, $n = 8$ independently prepared electrodes), and retained 81.55% of its initial response after 55 days of storage. In addition, the platform showed strong anti-interference behavior and delivered accurate quantification in spiked human urine and serum, achieving recoveries of 95.6–107.6% with precision better than 3.29% RSD, supporting its applicability in complex biological matrices. Overall, the Ag–Sn@MOFs/GCE sensor provides a sensitive and robust electroanalytical route for VIS monitoring in bioanalytical contexts. Future efforts should prioritize validation in authentic patient specimens, expanded cross-reactivity evaluation against structurally and therapeutically related anticancer agents, and translation into portable and multiplexed formats to broaden clinical and point-of-care utility.

Ethical statement

In compliance with Egyptian regulations, the study received ethical clearance from Assiut University and included only participants who had provided informed consent.

Conflicts of interest

The authors declare no competing interests.

Data availability

Data will be available upon request from the corresponding author.

Supplementary information (SI) is available. See DOI: https://doi.org/10.1039/d6ra01976e.

Acknowledgements

This work was supported and funded by the Deanship of Scientific Research at Imam Mohammad Ibn Saud Islamic University (IMSIU) (grant number IMSIU-DDRSP2601).

References

1 D. Hanahan and R. A. Weinberg, *Cell*, 2011, **144**, 646–674.
2 F. Bray, J. Ferlay, I. Soerjomataram, R. L. Siegel, L. A. Torre and A. Jemal, *CA Cancer J. Clin.*, 2018, **68**, 394–424.
3 D. S. Shewach and R. D. Kuchta, *Chem. Rev.*, 2009, **109**, 2859–2861.
4 C. M. Rudin, Vismodegib, *Clin. Cancer Res.*, 2012, **18**, 3218–3222.
5 M. R. Sharma, T. G. Karrison, B. Kell, K. Wu, M. Turcich, D. Geary, S. P. Kang, N. Takebe, R. A. Graham, M. L. Maitland, R. L. Schilsky, M. J. Ratain and E. E. W. Cohen, *Clin. Cancer Res.*, 2013, **19**, 3059–3067.

6 E. H. Epstein, *Nat. Rev. Cancer*, 2008, **8**, 743–754.
7 Y. Deng, H. Wong, R. A. Graham, W. Liu, H. Shen, Y. Shi, L. Wang, M. Meng, V. Malhi, X. Ding and B. Dean, *J. Chromatogr. B*, 2011, **879**, 2119–2126.
8 P. Claire, H. Huu-Hien, P. Alain, S. Hélène, M. Isabelle, C. Cécile, L. Maignan, C. M. Samia and G. Lauriane, *Ther. Drug Monit.*, 2018, **40**, 337–343.
9 P. S. Pulusu and P. Kommarajuia, *J. Chromatogr. Sep. Tech.*, 2019, **10**, 421.
10 V. M. Goud, M. Harini, C. H. B. P. Devi and M. M. Goud, *J. Pharm. Res. Int.*, 2021, **33**, 858–866.
11 A. M. Mahmoud, M. H. Mahnashi, A. Al Fatease, M. A. H. Mostafa, M. M. El-Wekil and R. Ali, *J. Food Compos. Anal.*, 2022, **108**, 104428.
12 R. M. K. Mohamed, S. H. Mohamed, A. M. Asran, I. H. Alsohaimi, H. M. A. Hassan, H. Ibrahim and M. M. El-Wekil, *Spectrochim. Acta, Part A*, 2023, **293**, 122444.
13 R. M. K. Mohamed, S. H. Mohamed, A. H. Alanazi, M. Alzaid, H. M. A. Hassan, H. Ibrahim and M. M. El-Wekil, *Microchem. J.*, 2026, **221**, 116768.
14 R. Ali, A. ZA Albalawi, A. H. Alahmadi, N. M. Alanazi, A. M. Humadi, M. H. Alatwi, A. H. Alharbi, E. M. Albalawi, F. M. Albalawi and M. M. El-Wekil, *Microchem. J.*, 2026, **220**, 116362.
15 M. Z. Abedeen, H. Laddha, M. Sharma, R. Gupta and H. S. Kushwaha, *J. Electroanal. Chem.*, 2923, **948**, 117810.
16 A. O. Alqarni, R. A. Alqahtani, A. M. Mahmoud, M. H. Almabadi, F. M. Alshareef, M. N. Goda, R. Ali and M. M. El-Wekil, *Microchem. J.*, 2025, **218**, 115794.
17 M. H. Mahnashi, A. M. Mahmoud, K. Alhazzani, A. Z. Alanazi, A. M. Alaseem, M. M. Algahtani and M. M. El-Wekil, *Microchim. Acta*, 2021, **188**, 124.
18 M. Jiang, J. Liao, C. Liu, J. Liu, P. Chen, J. Zhou, Z. Du, Y. Liu, Y. Luo, Y. Liu, F. Chen, X. Fang and X. Lin, *Bioeng. Biotechnol.*, 2023, **11**, 1251713.
19 M. K. Muthukumaran, M. Govindaraj, S. Kogularasu, B. Sriram, B. K. Raja, S.-F. Wang, G.-P. Chang-Chien and A. Selvi, *Talanta Open*, 2025, **11**, 100396.
20 S. Rani S, B. Sharma, R. Malhotra, S. Kumar, R. S. Varma and N. Dilbaghi, *Environ. Res.*, 2020, **191**, 110005.
21 J. Cao, J. Yun, N. Zhang, Y. Wei, H. Yang and Z. Xu, *Synth. Met.*, 2021, **282**, 116931.
22 C. Zhang, L. Li, J. Ju and W. Chen, *Electrochim. Acta*, 2016, **210**, 181–189.
23 X. Lu, F. Luo, Q. Xiong, H. Chi, H. Qin, Z. Ji, L. Tong and H. Pan, *Mater. Res. Bull.*, 2018, **99**, 45–51.
24 P. Arul and S. A. John, *Electrochim. Acta*, 2017, **235**, 680–689.
25 Y. Zhang, Z. Wang, S. Liu and T. Zhang, *Mater. Res. Bull.*, 2016, **84**, 355–362.
26 P. Paulraj, A. Umar, K. Rajendran, A. Manikandan, R. Kumar, E. Manikandan, K. Pandian, M. H. Mahnashi, M. A. Alsaiari, A. A. Ibrahim, N. Bouropoulos and S. Baskoutas, *Electrochim. Acta*, 2020, **363**, 137158.
27 L. Yadav, P. Yadav, H. Laddha, M. Sharma, P. Sharma, M. Agarwal and R. Gupta, *Inorg. Chem. Commun.*, 2024, **161**, 112083.
28 M. Kasula, T. Le, A. Thomsen and M. R. Esfahani, *Chem. Eng. J.*, 2022, **439**, 135542.
29 H. Laddha, P. Sharma, N. B. Jadhav, M. Z. Abedeen and R. Gupta, *Langmuir*, 2023, **39**, 17756–17769.
30 R. A. Molla, K. Ghosh, B. Banerjee, M. A. Iqubal, S. K. Kundu, S. M. Islam and A. Bhaumik, *J. Colloid Interface Sci.*, 2016, **477**, 220–229.
31 D.-H. Wu, H. Huang, M. U. Haq, L. Zhang, J.-J. Feng and A.-J. Wang, *J. Colloid Interface Sci.*, 2023, **647**, 1–11.
32 R. Jesuraj, A. Amalraj, V. K. Vaidyanathan and P. Perumal, *Analyst*, 2023, **148**, 5157–5171.
33 Y. S. Alqahtani, A. M. Mahmoud, M. H. Mahnashi, R. Ali, R. Y. Shahin, M. M. El-Wekil and H. A. Batakoushy, *RSC Adv.*, 2023, **13**, 23736–23744.
34 S. P. Lim, A. Pandikumar, H. N. Lim, R. Ramaraj and N. M. Huang, *Sci. Rep.*, 2015, **5**, 11922.
35 H. Song, L. Zhang, C. He, Y. Qu, Y. Tian and Y. Lv, *J. Mater. Chem.*, 2011, **21**, 5972–5977.
36 A. K. Chen, H. Zhao, Z. Wang, F. Zhou, Z. Shi, S. Cao and M. Lan, *Biosens. Bioelectron.*, 2022, **212**, 114431.
37 M. M. El-Wekil, A. M. Hayallah, M. A. Abdelgawad, M. A. S. Abourehab and R. Y. Shahin, *J. Electroanal. Chem.*, 2022, **922**, 116745.
38 S. A. Alkahtani, A. M. Mahmoud and M. M. El-Wekil, *Electroanal. Chem.*, 2022, **908**, 116102.
39 A. Z. Alanazi, K. Alhazzani, H. Ibrahim, A. B. H. Ali, M. Darweesh and M. M. El-Wekil, *Anal. Methods*, 2024, **16**, 7234–7241.
40 J. Lakshmikantha, G. Krishnamurthy, R. H. Nayak, M. Pari, N. Ranjitha and N. Naik, *Inorg. Chem. Commun.*, 2022, **146**, 110175.
41 M. H. Yildir, A. A. Genc, N. Erk, W. Bouali, N. Bugday, S. Yasar and O. Duygulu, *Microchim. Acta*, 2024, **191**, 221.
42 H. Ibrahim and Y. Temerk, *Microchim. Acta*, 2020, **187**, 1–11.
43 M. Nawaz, H. Shaikh, J. A. Buledi, A. R. Solangi, C. Karaman, N. Erk, R. Darabi and M. B. Camarada, *Carbon Lett.*, 2024, **34**, 201–214.
44 A. M. Mahmoud, M. H. Mahnashi and M. M. El-Wekil, *Talanta*, 2021, **221**, 121562.
45 G. K. Abou-Alfa, L. D. Lewis, P. LoRusso, M. Maitland, P. Chandra, S. Cheeti, D. Colburn, S. Williams, B. Simmons and R. A. Graham, *Cancer Chemother. Pharmacol.*, 2017, **80**, 29–36.
46 R. A. Graham, B. L. Lum, G. Morrison, I. Chang, K. Jorga, B. Dean, Y. G. Shin, Q. Yue, T. Mulder, V. Malhi and M. Xie, *Drug Metab. Dispos.*, 2011, **39**, 1460–1467.
47 A. M. Alaseem, R. Orfali, G. Alasiri, R. Ali, A. B. H. Ali and M. M. El-Wekil, *Anal. Methods*, 2026, **18**, 1937–1947.
48 B. Hosseinzadeh, S. Irem Kaya, A. Çetinkaya, E. B. Atici and S. A. Ozkan, *Talanta*, 2024, **278**, 126510.
49 B. Chen, J. Xu, Q. Chen, H. Wu, B. Ou, Z. Zhou, F. Xu, S. Wu and S. Xie, *Eur. J. Drug Metab. Pharmacokinet.*, 2024, **49**, 645–655.